ACS central science

Research Article

Cite This: ACS Cent. Sci. 2018, 4, 1495−1502

http://pubs.acs.org/journal/acscii

Highly Oriented Liquid Crystal Semiconductor for Organic Field-Effect Transistors

Moon Jong Han,[†,○] Dayan Wei,[‡,○] Yun Ho Kim,[§] Hyungju Ahn,[∥] Tae Joo Shin,[⊥] Noel A. Clark,[#] David M. Walba,[*,‡] and Dong Ki Yoon[*,†,▽]

[†]Graduate School of Nanoscience and Technology, Korea Advanced Institute of Science and Technology, Daejeon 34141, Republic of Korea

[‡]Department of Chemistry and Biochemistry, Soft Materials Research Center, University of Colorado, Boulder, Colorado 80309, United States

[§]Advanced Functional Materials Research Group, KRICT, Daejeon 34114, Republic of Korea

[∥]Pohang Accelerator Laboratory, POSTECH, Pohang 37673, Republic of Korea

[⊥]UNIST Central Research Facilities & School of Natural Science, UNIST, Ulsan 44919, Republic of Korea

[#]Department of Physics and Soft Materials Research Center, University of Colorado, Boulder, Colorado 80309, United States

[▽]Department of Chemistry and KINC, Korea Advanced Institute of Science and Technology, Daejeon 34141, Republic of Korea

Supporting Information

ABSTRACT: We report a mesogenic compound which introduces nematic liquid crystal (LC) ordering into the benzothienobenzothiophene (BTBT) family of LCs, creating a new class of LC semiconducting materials which respond in a facile way to anisotropic surfaces, and can, thereby, be effectively processed into highly oriented monodomains. Measurement on these domains of the electrical conductivity, with in situ monitoring of domain quality and orientation using LC birefringence textures in electroded cells, brings a new era of precision and reliability to the determination of anisotropic carrier mobility in LC semiconductors.

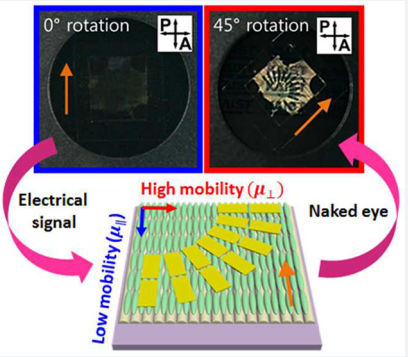

INTRODUCTION

One of the prototypical organic electronic devices is the field-effect transistor (FET), which has been widely used in many electronic devices, including displays,[1−5] sensors,[6−8] imagers,[9,10] radio frequency identification (RFID), and logic elements.[11−13] Recent research has shown that small-molecule organic semiconductors (OSCs) possessing liquid crystal (LC) phases are of great potential value in FET devices owing to their flexibility, tunability, proven efficacy in large-area thin-film devices, ability to operate over a wide temperature range, low cost, and solution-processability when compared to organic polymer and inorganic semiconductors.[14−17] However, prior reports regarding LC OSCs have not taken advantage of several valuable inherent properties of LC phases, specifically the well-known capability of many LCs to be "aligned" uniformly to improve the device performance and, in the context of this work, the OSC charge-carrier mobility in thin films. For example, previous research on LC OSCs focused on the smectic E phase, which is a highly ordered solidlike phase that uses spin-coating from a solution followed by thermal annealing to improve the charge-carrier mobility.[18]

The use of conventional spin-coating, which gives unaligned samples, may be driven by the difficulty in realizing the alignment of the LC OSCs investigated using conventional LC alignment methods.[19−21] However, many other complex fabrication tools, including solvent-exchange methods,[22] evaporation-induced self-assembly,[23] vapor deposition,[24] and template-assisted self-assembly,[25] have been shown to allow the formation of aligned smectic LC samples to some degree. In addition to these, some solution-processable LC OSC alignment has been demonstrated using solvent-assisted methods such as soft lithography,[26] off-center spin-coating,[27] antisolvent crystallization,[28] zone casting,[29] and solution shearing.[30] All of these limitations are due to the disorder in the molecular arrangement as solvent dries, resulting in unintended or uncontrollable morphologies such as grain boundaries, glasslike structures, and phase segregation, which can deteriorate the electrical property. Furthermore, it is not easy to align LC OSCs with uniaxial planar configuration because the solution-processed open-cell system induces

Received: July 15, 2018
Published: October 24, 2018

DOI: 10.1021/acscentsci.8b00465
ACS Cent. Sci. 2018, 4, 1495−1502

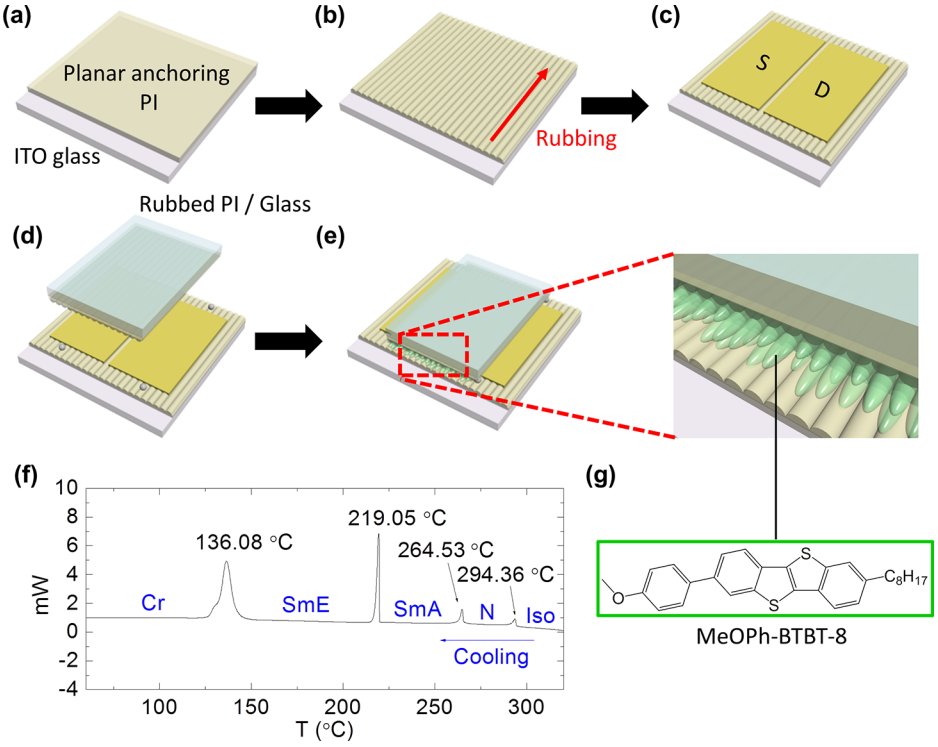

Figure 1. Schematic illustration of the bottom-gate bottom-contact OFET fabrication process. (a) Planar anchoring polyimide solution was spin-coated on ITO-coated glass. (b) The rubbing method is treated on PA PI layer. (c) Au electrodes were thermally evaporated on the rubbed PI dielectric layer followed by fabrication of the PFBT SAM layer. (d) The top substrate was flipped over on the prepared bottom substrate followed by UV exposure to control the cell gap using silica particles dissolved in UV-curable glue. (e) The sandwich cell is filled with LC materials by capillary force near the nematic to the isotropic phase-transition temperature of ~280 °C. (f) DSC curves were obtained at 5 °C min^{-1} for the cooling process. (g) Chemical structure of MeOPh-BTBT-8.

majorly vertically oriented films due to the strong homeotropic anchoring manner of air. However, like the most solvent-free or melt-fluidic LC phase, the nematic LC phase can provide very high-quality alignment. Additionally possessing only long-range orientational order, it allows the uniaxial planar alignment under rubbed planar anchoring conditions over large areas. This feature is fundamental to the realization of the now ubiquitous LC display (LCD).[31] It may also be advantageous to organic light-emitting diodes (OLEDs) integrated with organic FETs (OFETs), where the light intensity is proportional to the charge-carrier mobility, so larger overlapped π orbitals and the uniformity of aligned organic semiconductor molecules are essential.[3,5]

Therefore, it is important to design new LC OSCs that can show both nematic and smectic phases. Here, we describe a new LC mesogen possessing the phase sequence nematic−smectic A−smectic E−crystal on cooling. Furthermore, we report the uniaxial planar alignment of the LC OSCs in rubbed planar anchoring sandwich cells in the nematic phase, and provide measurements of the anisotropic charge-carrier mobility and birefringence intensity in the LC phases. This work demonstrates a strong correlation between the birefringent brightness, which is a directly visible measure of the LC anisotropic orientation, and the charge-carrier mobility.

RESULTS AND DISCUSSION

FET Device Fabrication and Molecule Design. To implement our strategy, we designed a modified planar anchoring sandwich cell as follows (Figure 1). First, a transparent indium-tin-oxide-coated (ITO-coated) glass substrate is treated by spin-coating with a polyimide (PI) "alignment layer" material expected to produce planar anchoring. This coating serves as both a dielectric and an alignment layer for the "bottom" substrate (Figure 1a). After uniaxial mechanical rubbing of the polyimide (PI) layer (a prototypical LC alignment method) (Figure 1b),[32,33] Au/Ti electrodes are deposited by conventional thermal evaporation through a metal shadow mask (Figure 1c). Then, a pentafluorobenzenethiol (PFBT) self-assembled monolayer is applied to reduce the contact resistance, which is important in the bottom-contact transistor configuration used for these experiments. The top substrate is prepared by spin-coating the PI on bare glass, followed by uniaxial rubbing to provide uniform planar alignment of LC OSC molecules (Figure 1d). To investigate the orientation of LC OSCs in our sandwich cell device, we investigated three different alignment conditions: (1) control without any rubbing process; (2) parallel-rubbed PI; and (3) perpendicular-rubbed PI; the latter two using orthogonal rubbing directions relative to the source/drain channel direction. Finally, similar to a conventional sandwich LC cell, an LC material is introduced between the top and bottom substrates at a temperature near the isotropic to nematic phase transition by capillary action, then cooled down at 15 °C min^{-1}. The film thickness (spacing between the substrate plates) is controlled using silica "spacer beads" dispersed in a UV-curable glue. In this study, the film thickness is approximately 1 μm. The final configuration of the resulting OFET is shown in Figure 1e. OFETs prepared in this way show highly uniform and smooth surfaces, and are composed of a pure organic compound, which is free of solvents. This is

DOI: 10.1021/acscentsci.8b00465
ACS Cent. Sci. 2018, 4, 1495−1502

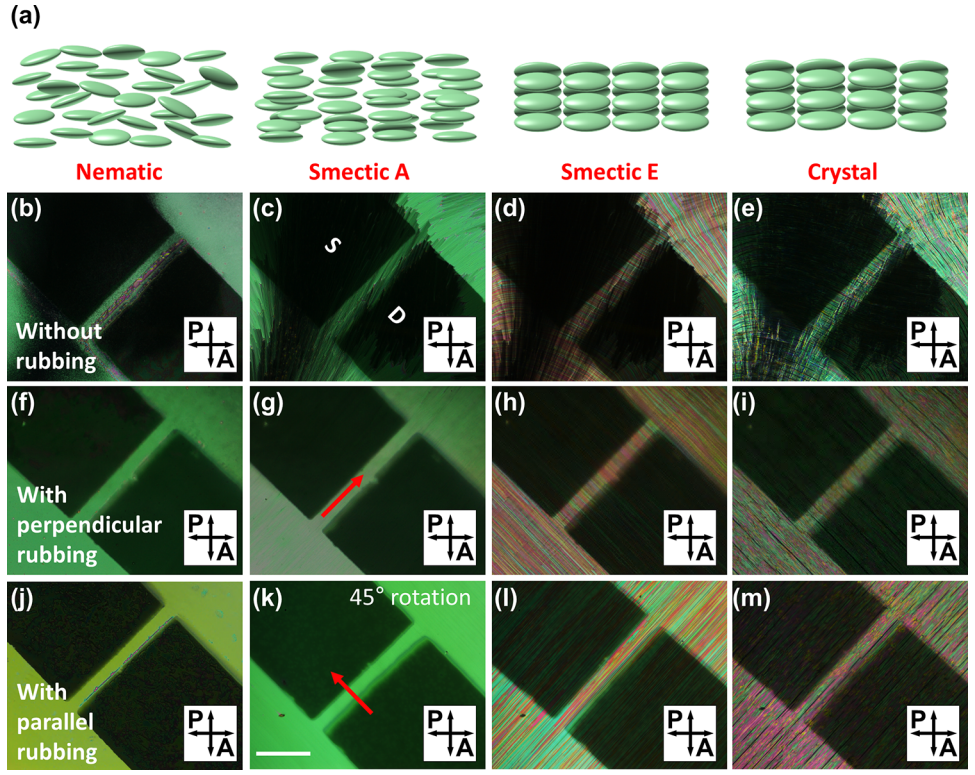

Figure 2. Series of POM images and structural hierarchy of different temperatures and rubbing conditions. (a) Structural hierarchy of MeOPh-BTBT-8 molecules in different phases. (b–e) POM images of different phases (smectic A, smectic E, and crystalline phase) with no rubbing condition. (f–i) POM images of different phases with rubbing direction perpendicular to source/drain channel direction. (j–m) POM images of different phases with rubbing direction parallel to source/drain channel direction. (Scale bar: 200 μm.)

important because the solvent evaporation can induce poor uniformity and rough surface morphology after the recrystallization. Our cell design and fabrication not only improve the reliability of the device performance, but also exhibit good reproducibility in terms of the FET performance, both from device to device and from sample to sample, showing minimal variation in FET mobility.

Existing well-established small-molecule LC OSCs are benzothienobenzothiophene (BTBT) derivatives.[23−26] One such a material is C8-BTBT, which possesses only a smectic A LC phase when two identical alkyl tails are symmetrically substituted on the BTBT core. Another well-known molecule is Ph-BTBT-10, which has an additional smectic E phase below the smectic A phase, obtained by replacing one of the flexible alkyl tails with a more rigid phenyl ring. On the basis of the BTBT core following some general trends regarding LC molecular design, a new LC OSC molecule 2-(4-methoxyphenyl)-7-octyl-benzothienobenzothiophene (MeOPh-BTBT-8) was prepared (Figure 1g). This material has a large π-conjugated fused ring structure to enhance the charge-carrier mobility and give a rigid mesogenic motif to form LC and crystal phases. The differential scanning calorimetry (DSC) chart (Figure 1f) shows the transition from isotropic to nematic, smectic A, smectic E, and crystal phases upon cooling, which is different from the previously reported asymmetric BTBT derivatives, which show only smectic A and smectic E phases.[18]

The detailed synthesis is shown in the Supporting Information (Figure S1).[34−36] The BTBT core is first synthesized, followed by the introduction of an *n*-octyl tail via a Friedel–Crafts acylation followed by Wolff–Kishner reduction. The resulting intermediate was then brominated (Br_2), followed by Suzuki coupling with 4-methoxy phenyl boronic acid to give a good yield of MeOPh-BTBT-8.

Polarized Optical Microscopic Properties of the New Mesogen. MeOPh-BTBT-8 exhibits three LC phases on cooling, which are directly observed by polarized optical microscopy (POM) (Figure 2). Figure 2a shows schematic representations of molecular packing in the nematic, smectic A, smectic E, and crystal phases. X-ray and electron diffraction structural studies of smectic E phase materials indicate a two-dimensional (2D) hexagonal lattice and strong herringbone packing.[37,38] For the current material, typical schlieren textures and uniaxial aligned single domains of the nematic phase in the sandwich cell device are observed without (Figure 2b) and with (Figure 2f,j) the rubbing process. The smectic A phase exhibits typical fan textures with disclination lines without rubbing (Figure 2c) at lower temperatures, while uniform and uniaxial single-domain alignment of LC OSCs can be seen when the rubbing direction is either perpendicular or parallel to the source/drain channel direction (Figure 2g,k). As expected, when the rubbing process is applied, the LC director is aligned with the rubbing direction (red arrows) in the nematic and smectic A phases. In the smectic E phase, stripe patterns are generated perpendicular to the molecular long axis orientation (Figure 2d,h,l), which results from close herringbone packing of the LC OSC molecules (Figure 2a). In addition, as expected, randomly oriented domains in the smectic E phase are generated when the PI is not rubbed (Figure 2d), meaning that molecular long axes are not macroscopically oriented. These alignment characteristics are also observed, even on cooling, to form the crystalline phase

DOI: 10.1021/acscentsci.8b00465
ACS Cent. Sci. 2018, 4, 1495−1502

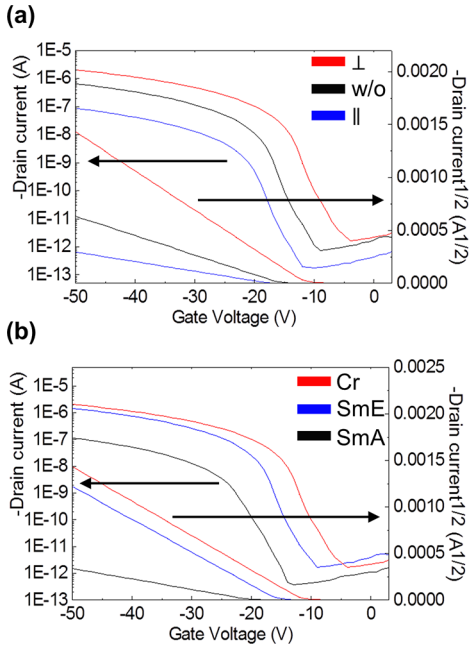

	Mobility ($cm^2V^{-1}s^{-1}$)	On/Off ratio	V_{th} (V)	S-slope (V/dec.)
w/o rubbing (w/o)	1.49	$8.85x10^5$	-16	3.41
Parallel (∥)	0.24	$5.04x10^5$	-19	3.92
Perpendicular (⊥)	3.80	$1.24x10^6$	-12	2.24

	Mobility ($cm^2V^{-1}s^{-1}$)	On/Off ratio	V_{th} (V)	S-slope (V/dec.)
Smectic A (240 °C)	0.28	$1.41x10^5$	-21	6.27
Smectic E (170 °C)	3.22	$8.86x10^5$	-15	2.95
Crystal (30 °C)	3.80	$1.24x10^6$	-12	2.24

Figure 3. Electrical characteristics of bottom-gate and bottom-contact FETs. (a) Transfer characteristics of FETs fabricated with rubbing directions that are different from the source/drain channel direction in the crystalline phase. (V_{SD} = −50 V) (b) Transfer characteristics of FETs fabricated with rubbing direction perpendicular to source/drain channel direction at different temperatures. (V_{SD} = −50 V).

(Figure 2e,i,m). Moreover, even in the crystalline phase, large cracks in the BTBT layer are not seen, suggesting a similar thermal expansion coefficient of lattices within the molecular layers in the smectic E and crystalline phases, as has been reported previously.[18,39,40] This results in an improvement in the reliability of FET devices fabricated with such materials.[18] Here, we show that the nematic phase at higher temperature is vital for the fabrication of unidirectional single-domain OFETs in rubbed sandwich cells, which is crucial for improving the device performance using LC OSCs. Without the nematic phase, LC OSCs with a direct phase transition from the isotropic to smectic phases are not well-aligned (Figures S2 and S3, Supporting Information) in planar anchored sandwich cells.

Electrical Properties As a Function of LC Director Orientation and Temperature. To measure the electrical properties, we used samples identical to those shown in Figure 2, and we obtained the results given in Figure 3 and Figures S4−S6 in the Supporting Information. The charge-carrier (which is, in this case, a hole) transfer characteristic of LC OSCs are generally believed to be governed by $\pi-\pi$ interactions between the aromatic cores (here, a herringbone arrangement of oriented MeOPh-BTBT-8 molecules), where the dominant $\pi-\pi$ packing direction is perpendicular to the rubbing direction. This means that holes transfer in the herringbone stacking direction.

Figure 3a shows the on/off ratio, threshold voltage, subthreshold slope, and the corresponding hole mobility for different rubbing orientations. Without the rubbed alignment layer, the mobility extracted from the transfer curve (black line in Figure 3a) is between the parallel and perpendicularly aligned LC OSCs because of the presence of both in- and out-of-plane $\pi-\pi$ stacking, which are better than only [001] directional (out-of-plane) charge-carrier transport and worse than [010] charge transport (in-plane). Additionally, the mobility value reported here is comparable to previously reported LC OSC-based OFETs.[23,24,41] However, we show here that the hole mobility ($\mu_\perp$) is the highest when the sample is rubbed perpendicular to the source/drain channel direction (red line in the graph), and $\mu_\parallel$ is the lowest when the alignment layer is rubbed parallel to the source/drain channel direction (blue line). Thus, the mobility shows anisotropy with respect to the orientation of the driving field relative to the LC director, of which anisotropy ratio ($\mu_\perp/\mu_\parallel$) is ∼15.83.

To study the molecular arrangement in more detail, 2D-grazing incidence X-ray diffraction (2D-GIXD) (Figure S7, Supporting Information) was performed on the MeOPh-BTBT-8 thin films under rubbed planar anchoring conditions. The diffraction peaks are typical for a crystalline phase, exhibiting the smectic E-like polar ordering modulated parallel to the substrate with face-on molecular orientation. It can be seen that the molecular long axis is oriented along the [001] direction, which coincides with the rubbing direction. The charge transport preferentially occurs along the [010] and [001] directions corresponding to perpendicular and parallel rubbing conditions, respectively. Meanwhile, in the previously reported device using C8-BTBT,[42] the peak corresponding to the [100] direction exhibits stronger intermolecular electronic coupling compared to the [010] direction. Although it is possible to further enhance the charge-carrier mobility by changing the device geometry or molecular orientation, it is difficult to align molecules along the [100] direction under homeotropic anchoring conditions because of the simple rod shape of the molecule used, which exhibits higher mobility and electrical anisotropy. It is to be noted that this is the first attempt to study high-quality alignment of solvent-free fluidic LC OSCs possessing a long-range orientational order resulting in uniaxial planar alignment in rubbed planar anchoring conditions over large areas.

We measured the temperature-dependent mobility to investigate the relationship between the molecular ordering and charge-carrier mobility. Figure 3b shows the hole-transfer

DOI: 10.1021/acscentsci.8b00465
ACS Cent. Sci. 2018, 4, 1495−1502

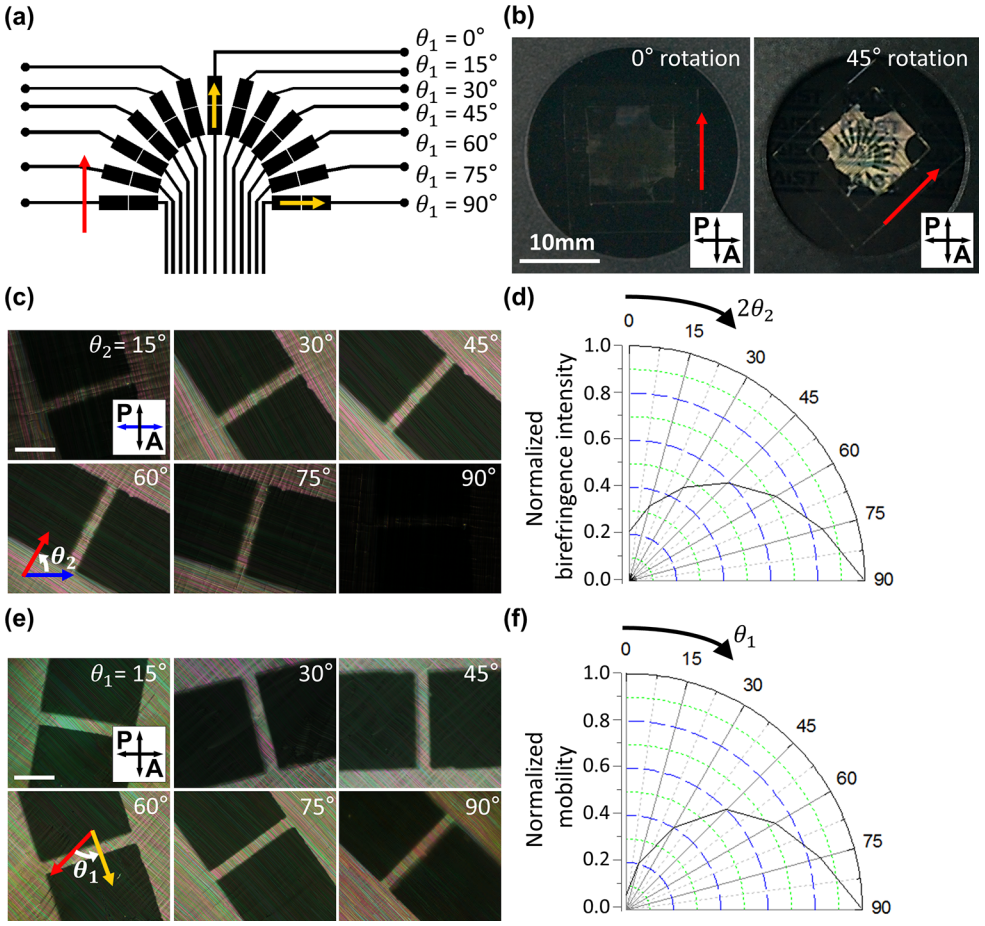

Figure 4. Fabrication of radial source/drain channel to evaluate orientation direction and hole-transfer mobility. (a) Schematic design of metal shadow mask to fabricate radial source/drain channel. θ_1 is the angle between the alignment direction (red) and source/drain channel direction (yellow). (b) Optical images of OFET based on modified sandwich cell under two polarizers. (c) POM images at a different angle (θ_2) between the fixed rubbing direction (red) and fixed polarizer direction (blue). (Scale bar: 40 μm.) (d) Birefringence intensity profile as a function of rotation angle ($2\theta_2$) between alignment direction and polarizer direction. (e) POM images at a different angle (θ_1) between the fixed rubbing direction (red) and source/drain channel direction (yellow). (Scale bar: 40 μm.) (f) Mobility profiles as a function of the angle (θ_1).

mobility in the different phases, i.e., smectic A, smectic E, and crystalline, when the perpendicularly rubbed alignment layer is used. Charge transport of smectic A, smectic E, and crystalline phases was measured at 240, 170, and 30 °C, respectively. As the molecular packing density increases with a decrease in temperature, a higher hole mobility is obtained, progressing from the smectic A to the crystal, as shown in Figure 3b. The electrical properties in nematic and isotropic phases are shown in Figure S4. An additional thermal annealing process on the sample at 140 °C was carried out for 5 min, which corresponds to the crystal−smectic E phase-transition temperature; then, the sample was cooled at 1 °C min^{-1}. This simple effort improves the FET mobility significantly from 3.58 to 9.5 cm^2 V^{-1} s^{-1} though the POM texture was little changed (Figure S8, Supporting Information). For a study of the origin of the increased performance after thermal annealing, out-of-plane XRD was carried out (Figure S8c, Supporting Information). The [002] peak intensity at q_z = 0.355 $Å^{-1}$ increases by 5 times after the annealing process, which means that thermal annealing generates the higher molecular ordering and consequently the higher charge-carrier mobility.[43−46] To evaluate the reliability and reproducibility of the FET performance of our platform, we measured the transfer characteristics for different rubbing conditions and temperatures with 10 bottom-gate and bottom-contact transistors on five substrates. As shown in Figure S8, the FET mobility and on/off ratio exhibit minimal variations because of the uniformity of the LC OSC films (Table S1, Supporting Information). Furthermore, the device stability is tested by irradiating the cell with UV light ($\lambda \approx 365$ nm, intensity ≈ 0.15 mW cm^{-2}) for approximately 12 h, as shown in Figure S9. The devices based on aligned MeOPh-BTBT-8 are very stable under these conditions, and exhibit little performance deterioration.

Molecular Arrangement and Source/Drain Angle-Dependent POM Images and Electrical Properties. Previously, LC OSCs and other organic FETs have been employed to maximize the charge-carrier mobility using various kinds of molecules and alignment methods.[25,27,28,47] In this study, we demonstrated the high-quality alignment of an LC OSC on a large length scale. To further study the anisotropy of charge transfer and the optical signals of LC samples (Figure 4), we describe the achievement of multi-channel source/drain electrodes on one LC cell sample. Here, the rubbing direction is fixed, and the channels have different angles [θ_1 relative to the rubbing direction, ranging from 0° to 90° in 15° increments (Figure 4a)]. This radial multichannel

DOI: 10.1021/acscentsci.8b00465
ACS Cent. Sci. 2018, 4, 1495−1502

device enables us to precisely test the hole mobility relative to the molecular long axis orientation.

For this, we examined the optical birefringence of the sample as it rotated between crossed polarizers (Figure 4b).[48,49] The LC OSC orientation can be simply analyzed using the resulting POM images because the transmitted light intensity (I) is proportional to $\sin^2 2\theta_2$, where θ_2 is the angle between the direction of the polarizer (P) and the rubbing direction. We measured the lowest transmittance when the rubbing direction was either parallel or perpendicular to the polarizer at $\theta_2 = 0°$ or 90°, respectively, while the highest transmittance is detected at $\theta_2 = 45°$ (Figure 4c). A polar plot of the uniaxially oriented LC OSC shows the first quadrant of a 4-fold symmetry pattern under crossed polarizers (Figure 4d). This plot shows the transmittance change of the sample as a function of θ_2. The change of transmittance exhibits a periodicity of 90°, revealing the maximum at $\theta_2 = 45°$. Then, we also measured the hole mobility (Figure 4e,f). A minimum mobility was obtained at $\theta_1 = 0°$ when the source-drain direction is parallel to the rubbing direction, while the maximum mobility was measured at $\theta_1 = 90°$. As a function of θ_1, the hole mobility is mapped out as shown in the polar plot (Figure 4f), in which the θ_1 increment induces the [010] direction of charge-carrier transports resulting in higher mobility.

In our system, both the birefringence and charge-carrier mobility show anisotropy in the LC OSC. By rotating the sample between the crossed polarizer and analyzer, we can easily determine the orientation of OSC molecules and the alignment quality, i.e., the direction, which is defined as directions, perpendicular or parallel to the rubbing direction, where the uniform highest brightness is detected at 45°, which corresponds to the molecule long axis. Then, we can visually tell the direction in which the charge-carrier mobility is the highest, which occurs when the source/drain channel direction is perpendicular to the rubbing direction. Although one-to-one correspondence cannot be made because the birefringence intensity is proportional to $2\theta_2$, and the charge-carrier mobility is proportional to θ_1, a follow-up study is in progress to make a one-to-one correspondence with the birefringence intensity seen when inserting a full λ plate. Thus, a visual observation without actually testing the charge-carrier mobility might directly indicate the highest charge-carrier mobility direction when the well-known LC OSC is used, which simplifies the device electrode-deposition process. In particular, upon fabrication of large numbers of OFETs, this visual guide would greatly improve the efficiency and reproducibility.

CONCLUSION

We have demonstrated a simple method for the fabrication of highly ordered and oriented supramolecular conducting LC materials, where an easy and extremely well-developed rubbing process can be used to align an LC material exhibiting the phase sequence nematic−smectic A−smectic E. The presence of the nematic phase, which is an LC phase widely used in displays, is the key property needed to realize the controllable uniaxial alignment of these LCs, facilitating the observation of significant changes in the charge-carrier mobility, depending on the rubbing direction and molecular long-axis orientation. We showed that the transmitted intensity is correlated with the charge-carrier mobility, which is useful for visual observation of the expected electrical signal. This general platform for the fabrication of OFETs provides an interesting way of studying the anisotropic charge-carrier behavior by employing a simple tool such as POM or two plastic crossed polarizers.

METHODS

Safety Statement. No unexpected or unusually high safety hazards were encountered.

Fabrication and Measurement of OFETs Based on Modified Sandwich Cell. The ITO glass for bottom substrates and bare glass for top substrates were cleaned using acetone and ethanol, followed by rinsing with deionized water. The cleaned ITO glass and bare glass were spin-coated with planar anchoring polyimide (PI, SE7492, Nissan chemical) followed by thermal annealing at 200 °C for 2 h. The bottom and top substrates were treated using the rubbing process using a rubbing machine (RMS-50-M, Namil Optics) for uniaxial alignment. The Au (40 nm)/Ti (5 nm) electrodes were deposited on the bottom substrate through a metal shadow mask via thermal evaporation. For fabrication of the self-assembly monolayer (SAM), the pentafluorobenzenethiol (PFBT, Sigma-Aldrich):ethanol solution (0.1 wt %) was spin-coated on the bottom substrates followed by thermal annealing at 120 °C for 1 h. For a uniform cell gap, the silicon particle with a 1 μm diameter was deposited on the edges of the bottom substrates using UV-curable polymer (NOA 63, Norland Products). The prepared top substrates were combined with the bottom substrates following UV exposure. The MeOPh-BTBT-8 crystalline powder was prepared on the entrance of the gap, and then heated to around the nematic phase temperature of MeOPh-BTBT-8 (T_N = 274 °C) to fill the sandwich cell by capillary action.

Imaging LC Structure in Sandwich Cells. Polarized optical microscopy (POM) (LV100POL, Nikon, Tokyo, Japan) was used to examine the optical textures of LC film at different temperatures. The birefringence intensity of the aligned LC films was quantitatively measured using a UV−vis spectroscopy (SPECTRA max Plus 384, Molecular Devices, Sunnyvale, CA) with a light source at 540 nm, in which the sandwich cells were rotated.

Molecular Structure Characterization. The grazing incidence X-ray diffraction (GIXD) experiments were performed at the 9A U-SAXS and 6D C&S UNIST-PAL beamlines of Pohang Accelerator Laboratory (PAL). The energy of the focused beam was 11.06 keV, and the sample-to-detector distance (SDD) was around 221.26 mm to observe the molecular and layer orientation. The diffraction patterns were recorded with a 2D CCD camera (Rayonix SX165).

Electrical Characterization. The transfer characteristics of the bottom-gate and bottom-contact FETs based on the LC semiconductor were characterized using a Keithley 4200 source measurement unit. The channel length (L)/width (W) ratio was 50/500 μm. The mobility (μ) was calculated by plotting the square root of the source-drain current (I_{DS}) versus the gate voltage (V_G), and using the following equation from the saturated region in the transfer curve:

$$I_{DS} = (WC_i/2L)\mu(V_G - V_{th})^2$$

where C_i is the capacitance per unit area of the gate insulator (~75 pF mm^{-2}), and V_{th} is the threshold voltage.

DOI: 10.1021/acscentsci.8b00465
ACS Cent. Sci. 2018, 4, 1495−1502

■ ASSOCIATED CONTENT

Supporting Information

The Supporting Information is available free of charge on the ACS Publications website at DOI: 10.1021/acscentsci.8b00465.

Additional data and figures including synthesis and fabrication schematics, transfer and output characteristics, 2D-GIXD patterns, and UV stability (PDF)

■ AUTHOR INFORMATION

Corresponding Authors

*E-mail: walba@colorado.edu.
*E-mail: nandk@kaist.ac.kr.

ORCID

Yun Ho Kim: 0000-0002-1722-5623
Dong Ki Yoon: 0000-0002-9383-8958

Author Contributions

○M.J.H. and D.W. contributed equally to this work. M.J.H., D.W., D.M.W., and D.K.Y. designed the research. M.J.H., D.W., H.A., and T.J.S. performed experimental works. M.J.H., D.W., Y.H.K., N.A.C., D.M.W., and D.K.Y. analyzed results and wrote the manuscript.

Notes

The authors declare no competing financial interest.

■ ACKNOWLEDGMENTS

This study was supported by a grant from the National Research Foundation (NRF) and funded by the Korean Government (MIST) (2017M3C1A3013923, 2017R1E1A1A01072798, and 2015M3A6A5065315). It was also supported by the Soft Materials Research Center under US NSF MRSEC Grant DMR-1420736.

■ REFERENCES

(1) Sheraw, C. D.; Zhou, L.; Huang, J. R.; Gundlach, D. J.; Jackson, T. N.; Kane, M. G.; Hill, I. G.; Hammond, M. S.; Campi, J.; Greening, B. K.; Francl, J.; West, J. Organic Thin-Film Transistor-Driven Polymer-Dispersed Liquid Crystal Displays on Flexible Polymeric Substrates. *Appl. Phys. Lett.* **2002**, *80*, 1088−1090.

(2) Rogers, J. A.; Bao, Z.; Baldwin, K.; Dodabalapur, A.; Crone, B.; Raju, V. R.; Kuck, V.; Katz, H.; Amundson, K.; Ewing, J.; Drzaic, P. Paper-like Electronic Displays: Large-Area Rubber-Stamped Plastic Sheets of Electronics and Microencapsulated Electrophoretic Inks. *Proc. Natl. Acad. Sci. U. S. A.* **2001**, *98*, 4835−4840.

(3) Zhou, L.; Park, S.; Bai, B.; Sun, J.; Wu, S.-C.; Jackson, T. N.; Nelson, S.; Freeman, D.; Hong, Y. Pentacene TFT Driven AM OLED Displays. *IEEE Electron Device Lett.* **2005**, *26*, 640−642.

(4) Zhou, L.; Wanga, A.; Wu, S.-C.; Sun, J.; Park, S.; Jackson, T. N. All-Organic Active Matrix Flexible Display. *Appl. Phys. Lett.* **2006**, *88*, 083502−083503.

(5) Yagi, I.; Hirai, N.; Miyamoto, Y.; Noda, M.; Imaoka, A.; Yoneya, N.; Nomoto, K.; Kasahara, J.; Yumoto, A.; Urabe, T. A Flexible Full-Color AMOLED Display Driven by OTFTs. *J. Soc. Inf. Disp.* **2008**, *16*, 15−20.

(6) Someya, T.; Sakurai, T. Integration of Organic Field-Effect Transistors and Rubbery Pressure Sensors for Artificial Skin Applications. *IEEE Int.* **2003**, 203−206.

(7) Kawaguchi, H.; Someya, T.; Sekitani, T.; Sakurai, T. Cut-and-Paste Customization of Organic FET Integrated Circuit and Its Application to Electronic Artificial Skin. *IEEE J. Solid-State Circuits* **2005**, *40*, 177−185.

(8) Stadlober, B.; Zirkl, M.; Leising, G. Transparent Pyroelectric Sensors and Organic Field-Effect Transistors with Fluorinated Polymers: Steps towards Organic Infrared Detectors. *IEEE Trans. Dielectr. Electr. Insul.* **2006**, *13*, 1087−1092.

(9) Someya, T.; Kato, Y.; Iba, S.; Noguchi, Y.; Sekitani, T.; Kawaguchi, H.; Sakurai, T. Integration of Organic FETs with Organic Photodiodes for a Large Area, Flexible, and Lightweight Sheet Image Scanners. *IEEE Trans. Electron Devices* **2005**, *52*, 2502−2511.

(10) Nausieda, I.; Ryu, K.; Kymissis, I.; Akinwande, A. I.; Bulović, V.; Sodini, C. G. An Organic Active-Matrix Imager. *IEEE Trans. Electron Devices* **2008**, *55*, 527−532.

(11) Drury, C. J.; Mutsaers, C. M. J.; Hart, C. M.; Matters, M.; de Leeuw, D. M. Low-Cost All-Polymer Integrated Circuits. *Appl. Phys. Lett.* **1998**, *73*, 108−110.

(12) Baude, P. F.; Ender, D. A.; Haase, M. A.; Kelley, T. W.; Muyres, D. V.; Theiss, S. D. Pentacene-Based Radio-Frequency Identification Circuitry. *Appl. Phys. Lett.* **2003**, *82*, 3964−3966.

(13) Myny, K.; Winckel, S. V.; Steudel, S.; Vicca, P.; De Jonge, S.; Beenhakkers, M. J.; Sele, C. W.; van Aerle, N. A. J. M.; Gelinck, G. H.; Genoe, J.; Heremans, P. An Inductively-Coupled 64b Organic RFID Tag Operating at 13.56 MHz with a Data Rate of 787 b/s. *In Solid-State Circuits Conf., 2008. ISSCC 2008. Digest of Technical Papers. IEEE Int.* **2008**, 290−614.

(14) Sundar, V. C.; Zaumseil, J.; Podzorov, V.; Menard, E.; Willett, R. L.; Someya, T.; Gershenson, M. E.; Rogers, J. A. Elastomeric Transistor Stamps: Reversible Probing of Charge Transport in Organic Crystals. *Science* **2004**, *303*, 1644−1646.

(15) Gundlach, D. J.; Royer, J. E.; Park, S. K.; Subramanian, S.; Jurchescu, O. D.; Hamadani, B. H.; Moad, A. J.; Kline, R. J.; Teague, L. C.; Kirillov, O.; Richter, C. A.; Kushmerick, J. G.; Richter, L. J.; Parkin, S. R.; Jackson, T. N.; Anthony, J. E. Contact-Induced Crystallinity for High-Performance Soluble Acene-Based Transistors and Circuits. *Nat. Mater.* **2008**, *7*, 216−221.

(16) Lezama, I. G.; Nakano, M.; Minder, N. A.; Chen, Z.; Di Girolamo, F. V.; Facchetti, A.; Morpurgo, A. F. Single-Crystal Organic Charge-Transfer Interfaces Probed Using Schottky-Gated Heterostructures. *Nat. Mater.* **2012**, *11*, 788−794.

(17) Giri, G.; Verploegen, E.; Mannsfeld, S. C.; Atahan-Evrenk, S.; Kim, D. H.; Lee, S. Y.; Becerril, H. A.; Aspuru-Guzik, A.; Toney, M. F.; Bao, Z. Tuning Charge Transport in Solution-Sheared Organic Semiconductors Using Lattice Strain. *Nature* **2011**, *480*, 504−508.

(18) Iino, H.; Usui, T.; Hanna, J. Liquid Crystals for Organic Thin-Film Transistors. *Nat. Commun.* **2015**, *6*, 6828.

(19) Ishihara, S.; Wakemoto, H.; Nakazima, K.; Matsuo, Y. The Effect of Rubbed Polymer-films on the Liquid-Crystal Alignment. *Liq. Cryst.* **1989**, *4*, 669−675.

(20) Kim, D. S.; Cha, Y. J.; Gim, M. J.; Yoon, D. K. Fast Fabrication of Sub-200-nm Nanogrooves Using Liquid Crystal Material. *ACS Appl. Mater. Interfaces* **2016**, *8*, 11851−11856.

(21) Gim, M. J.; Yoon, D. K. Orientation Control of Smectic Liquid Crystals via a Combination Method of Topographic Patterning and In-Plane Electric Field Application for a Linearly Polarized Illuminator. *ACS Appl. Mater. Interfaces* **2016**, *8*, 27942−27948.

(22) Oh, J. H.; Lee, H. W.; Mannsfeld, S.; Stoltenberg, R. M.; Jung, E.; Jin, Y. W.; Kim, J. M.; Yoo, J. B.; Bao, Z. Solution-Processed, High-Performance N-Channel Organic Microwire Transistors. *Proc. Natl. Acad. Sci. U. S. A.* **2009**, *106*, 6065−6070.

(23) Zhang, C.; Zhang, X.; Zhang, X.; Fan, X.; Jie, J.; Chang, J. C.; Lee, C.-S.; Zhang, W.; Lee, S.-T. Facile One-Step Growth and Patterning of Aligned Squaraine Nanowires via Evaporation-Induced Self-Assembly. *Adv. Mater.* **2008**, *20*, 1716−1720.

(24) Adler-Abramovich, L.; Aronov, D.; Beker, P.; Yevnin, M.; Stempler, S.; Buzhansky, L.; Rosenman, G.; Gazit, E. Self-Assembled Arrays of Peptide Nanotubes by Vapour Deposition. *Nat. Nanotechnol.* **2009**, *4*, 849−854.

(25) Kim, A.; Jang, K. S.; Kim, J.; Won, J. C.; Yi, M. H.; Kim, H.; Yoon, D. K.; Shin, T. J.; Lee, M. H.; Ka, J. W.; Kim, Y. H. Solvent-Free Directed Patterning of a Highly Ordered Liquid Crystalline Organic Semiconductor via Template-Assisted Self-Assembly for Organic Transistors. *Adv. Mater.* **2013**, *25*, 6219−6225.

DOI: 10.1021/acscentsci.8b00465
ACS Cent. Sci. 2018, 4, 1495−1502

(26) Jo, P. S.; Vailionis, A.; Park, Y. M.; Salleo, A. A. Scalable Fabrication of Strongly Textured Organic Semiconductor Micropatterns by Capillary Force Lithography. *Adv. Mater.* **2012**, *24*, 3269−3274.
(27) Yuan, Y.; Giri, G.; Ayzner, A. L.; Zoombelt, A. P.; Mannsfeld, S. C.; Chen, J.; Nordlund, D.; Toney, M. F.; Huang, J.; Bao, Z. Ultra-High Mobility Transparent Organic Thin Film Transistors Grown by An Off-Centre Spin-Coating Method. *Nat. Commun.* **2014**, *5*, 3005.
(28) Minemawari, H.; Yamada, T.; Matsui, H.; Tsutsumi, J.; Haas, S.; Chiba, R.; Kumai, R.; Hasegawa, T. Inkjet Printing of Single-Crystal Films. *Nature* **2011**, *475*, 364−367.
(29) Janneck, R.; Vercesi, F.; Heremans, P.; Genoe, J.; Rolin, C. Predictive Model for the Meniscus-Guided Coating of High-Quality Organic Single-Crystalline Thin Films. *Adv. Mater.* **2016**, *28*, 8007−8013.
(30) Diao, Y.; Tee, B. C.; Giri, G.; Xu, J.; Kim, D. H.; Becerril, H. A.; Stoltenberg, R. M.; Lee, T. H.; Xue, G.; Mannsfeld, S. C.; Bao, Z. Solution Coating of Large-Area Organic Semiconductor Thin Films with Aligned Single-Crystalline Domains. *Nat. Mater.* **2013**, *12*, 665−671.
(31) Ryu, S. H.; Yoon, D. K. Molecular Orientation of Liquid Crystals on Topographic Nanopatterns. *ACS Appl. Mater. Interfaces* **2016**, *8*, 17707−17712.
(32) Wu, D.; Kaplan, M.; Ro, H. W.; Engmann, S.; Fischer, D. A.; DeLongchamp, D. M.; Richter, L. J.; Gann, E.; Thomsen, L.; McNeill, C. R.; Zhang, X. Blade Coating Aligned, High-Performance, Semiconducting-Polymer Transistors. *Chem. Mater.* **2018**, *30*, 1924−1936.
(33) Tseng, H. R.; Ying, L.; Hsu, B. B. Y.; Perez, L. A.; Takacs, C. J.; Bazan, G. C.; Heeger, A. J. High Mobility Field Effect Transistors Based on Macroscopically Oriented Regioregular Copolymers. *Nano Lett.* **2012**, *12*, 6353−6357.
(34) Saito, M.; Osaka, I.; Miyazaki, E.; Takimiya, K.; Kuwabara, H.; Ikeda, M. One-Step Synthesis of [1]benzothieno[3,2-b][1]-benzothiophene from o-chlorobenzaldehyde. *Tetrahedron Lett.* **2011**, *52*, 285−288.
(35) Ebata, H.; Izawa, T.; Miyazaki, E.; Takimiya, K.; Ikeda, M.; Kuwabara, H.; Yui, T. Highly Soluble [1]Benzothieno[3,2-b]-benzothiophene (BTBT) Derivatives for High-Performance, Solution-Processed Organic Field-Effect Transistors. *J. Am. Chem. Soc.* **2007**, *129*, 15732−15733.
(36) Inoue, S.; Minemawari, H.; Tsutsumi, J. y.; Chikamatsu, M.; Yamada, T.; Horiuchi, S.; Tanaka, M.; Kumai, R.; Yoneya, M.; Hasegawa, T. Effects of Substituted Alkyl Chain Length on Solution-Processable Layered Organic Semiconductor Crystals. *Chem. Mater.* **2015**, *27*, 3809−3812.
(37) Pershan, P. S. *Structure of Liquid Crystals*; World Scientific Publishing Co. Pty. Ltd.: Singapore, 1988.
(38) Stoebe, T.; Huang, C. C. Nature of the Smectic-A−Hexatic-B−Crystal-E transitions in extremely Thin Films Determined by Optical Reflectivity Measurements. *Phys. Rev. E: Stat. Phys., Plasmas, Fluids, Relat. Interdiscip. Top.* **1994**, *49*, 5238−5242.
(39) Yoon, D. K.; Choi, M. C.; Kim, Y. H.; Kim, M. W.; Lavrentovich, O. D.; Jung, H. T. Internal Structure Visualization and Lithographic Use of Periodic Toroidal Holes in Liquid Crystals. *Nat. Mater.* **2007**, *6*, 866−870.
(40) Honglawan, A.; Beller, D. A.; Cavallaro, M.; Kamien, R. D.; Stebe, K. J.; Yang, S. Topographically Induced Hierarchical Assembly and Geometrical Transformation of Focal Conic Domain Arrays in Smectic Liquid Crystals. *Proc. Natl. Acad. Sci. U. S. A.* **2013**, *110*, 34−39.
(41) Li, Y.; Liu, C.; Kumatani, A.; Darmawan, P.; Minari, T.; Tsukagoshi, K. Large Plate-like Organic Crystals from Direct Spin-Coating for Solution-Processed Field-Effect Transistor Arrays with High Uniformity. *Org. Electron.* **2012**, *13*, 264−272.
(42) Izawa, T.; Miyazaki, E.; Takimiya, K. Molecular Ordering of High-Performance Soluble Molecular Semiconductors and Re-evaluation of Their Field-Effect Transistor Characteristics. *Adv. Mater.* **2008**, *20*, 3388−3392.
(43) Kim, S.; Kim, A.; Jang, K.-S.; Yoo, S.; Ka, J.-W.; Kim, J.; Yi, M. H.; Won, J. C.; Hong, S.-K.; Kim, Y. H. The Effect of Thermal Annealing on the Layered Structure of Smectic Liquid Crystalline Organic Semiconductor on Polyimide Gate Insulator and Its OFET Performance. *Synth. Met.* **2016**, *220*, 311−217.
(44) DeLongchamp, D. M.; Kline, R. J.; Jung, Y.; Germack, D. S.; Lin, E. K.; Moad, A. J.; Richter, L. J.; Toney, M. F.; Heeney, M.; McCulloch, I. Controlling the Orientation of Terraced Nanoscale "Ribbons" of a Poly(Thiophene) Semiconductor. *ACS Nano* **2009**, *3*, 780−787.
(45) He, Y.; Sezen, M.; Zhang, D.; Li, A.; Yan, L.; Yu, H.; He, C.; Goto, O.; Loo, Y. L.; Meng, H. High Performance OTFTs Fabricated Using a Calamitic Liquid Crystalline Material of 2-(4-Dodecyl phenyl)[1]benzothieno[3,2-b][1]benzothiophene. *Adv. Electron. Mater.* **2016**, *2*, 1600179.
(46) DeLongchamp, D. M.; Kline, R. J.; Jung, Y.; Germack, D. S.; Lin, E. K.; Moad, A. J.; Richter, L. J.; Toney, M. F.; Heeney, M.; McCulloch, I. Controlling the Orientation of Terraced Nanoscale "Ribbons" of a Poly(thiophene) Semiconductor. *ACS Nano* **2009**, *3*, 780−787.
(47) Luo, C.; Kyaw, A. K.; Perez, L. A.; Patel, S.; Wang, M.; Grimm, B.; Bazan, G. C.; Kramer, E. J.; Heeger, A. J. General Strategy for Self-Assembly of Highly Oriented Nanocrystalline Semiconducting Polymers with High Mobility. *Nano Lett.* **2014**, *14*, 2764−2771.
(48) Kleinhenz, N.; Persson, N.; Xue, Z.; Chu, P. H.; Wang, G.; Yuan, Z.; McBride, M. A.; Choi, D.; Grover, M. A.; Reichmanis, E. Ordering of Poly(3-Hexylthiophene) in Solutions and Films: Effects of Fiber Length and Grain Boundaries on Anisotropy and Mobility. *Chem. Mater.* **2016**, *28*, 3905−3913.
(49) James, D. T.; Kjellander, B. K. C.; Smaal, W. T. T.; Gelinck, G. H.; Combe, C.; McCulloch, I.; Wilson, R.; Burroughes, J. H.; Bradley, D. D. C.; Kim, J. S. Thin-Film Morphology of Inkjet-Printed Single-Droplet Organic Transistors Using Polarized Raman Spectroscopy: Effect of Blending Tips-Pentacene with Insulating Polymer. *ACS Nano* **2011**, *5*, 9824−9835.

DOI: 10.1021/acscentsci.8b00465
ACS Cent. Sci. 2018, 4, 1495−1502